Truncated RNA-binding protein production by DUX4-induced systemic inhibition of nonsense-mediated RNA decay

Amy E. Campbell[1*], Michael C. Dyle[1*], Lorenzo Calviello[2*], Tyler Matheny[3], Kavitha Sudheendran[4], Michael A. Cortazar[1], Thomas Forman[5,6], Rui Fu[3], Austin E. Gillen[3], Marvin H. Caruthers[4], Stephen N. Floor[7,8], and Sujatha Jagannathan[1,3†]

[1]Department of Biochemistry and Molecular Genetics, University of Colorado Anschutz Medical Campus, Aurora, CO 80045, USA.
[2]Human Technopole, Milan, Italy.
[3]RNA Bioscience Initiative, University of Colorado Anschutz Medical Campus, Aurora, CO 80045, USA.
[4]Department of Biochemistry, University of Colorado Boulder, Boulder, CO 80309, USA.
[5]Department of Craniofacial Biology, University of Colorado Anschutz Medical Campus, Aurora, CO 80045, USA.
[6]Medical Scientist Training Program, University of Colorado Anschutz Medical Campus, Aurora, CO 80045, USA.
[7]Department of Cell and Tissue Biology, University of California, San Francisco, San Francisco, CA 94143, USA.
[8]Helen Diller Family Comprehensive Cancer Center, University of California, San Francisco, San Francisco, CA 94143, USA.

*These authors contributed equally
[†]Correspondence: sujatha.jagannathan@cuanschutz.edu

Running title: NMD inhibition induces truncated proteins

Keywords: NMD, DUX4, FSHD, translation, splicing

ABSTRACT

Nonsense-mediated RNA decay (NMD) is a surveillance mechanism that degrades both canonical and aberrant transcripts carrying premature translation termination codons. NMD is thought to have evolved to prevent the synthesis of toxic truncated proteins. However, whether global inhibition of NMD results in widespread production of truncated proteins is unknown. A human genetic disease, facioscapulohumeral muscular dystrophy (FSHD) features acute inhibition of NMD upon expression of the disease-causing transcription factor, DUX4. Here, using a cell-based model of FSHD, we show the production of hundreds of truncated proteins from physiological NMD targets. Using ribosome profiling, we map the precise C-terminal end of these aberrant truncated proteins and find that RNA-binding proteins are especially enriched for aberrant truncations. The stabilized NMD isoform of one RNA-binding protein, SRSF3, is robustly translated to produce a stable truncated protein, which can also be detected in FSHD patient-derived myotubes. Notably, ectopic expression of truncated SRSF3 alone confers toxicity and its downregulation is cytoprotective. Our results demonstrate the genome-scale impact of NMD inhibition. This widespread production of potentially deleterious truncated proteins has implications for FSHD biology as well as other genetic diseases where NMD is therapeutically modulated.

INTRODUCTION

Nonsense-mediated RNA decay (NMD) degrades transcripts containing premature termination codons (PTCs) that arise from nonsense mutations or RNA processing errors. Through this mechanism, NMD prevents the production of potentially toxic truncated proteins [1]. In addition to its role as a quality control mechanism, NMD also serves to regulate the expression of physiological transcripts that mimic NMD substrates. Such transcripts include a cassette exon containing a PTC, upstream open reading frames, or long 3' untranslated regions. Additionally, intricate auto- and cross-regulatory feedback loops have evolved that utilize NMD to titrate the level of various splicing factors. An excess amount of these splicing factors facilitates the inclusion of a PTC-containing exon which reduces gene expression ("unproductive splicing") [2, 3]. Due to its dual role as a quality control and gene regulatory mechanism, NMD efficiency is modulated in a variety of physiological contexts including cell stress, differentiation, and development [4-7]. NMD is also therapeutically targeted to allow the production of certain truncated proteins that retain residual function to counter loss-of-function genetic diseases [8]. In both scenarios, it remains an open question whether NMD inhibition has broader deleterious consequences for the cell.

Depletion of proteins involved in NMD, as well as pharmacological inhibition of NMD, has been shown to upregulate thousands of aberrant transcripts that are typically degraded by NMD [1, 9-11]. However, whether such transcripts produce truncated proteins is not known. At an organismal level, NMD inhibition has been shown to be immunogenic [12, 13], hinting at the production of truncated proteins with neoantigenic epitopes, although the identity of such proteins has not been characterized.

In this study, we took advantage of a cellular model of a human genetic disease, facioscapulohumeral muscular dystrophy (FSHD), where NMD is naturally inhibited and therefore we could investigate the molecular and functional consequences of the loss of NMD. FSHD is a prevalent progressive myopathy caused by misexpression of a double homeodomain transcription factor, DUX4, in skeletal muscle [14, 15]. DUX4 is normally expressed during early embryonic development where it activates the first wave of zygotic gene expression [16-18]. However, in individuals with FSHD, DUX4 is reactivated in the muscle and induces apoptotic death leading to skeletal muscle atrophy [19-22]. We have shown that DUX4 misexpression in

78 muscle cells causes rapid and acute inhibition of NMD followed by proteotoxic stress and,
79 eventually, translation inhibition [23, 24].
80
81 Here, we asked whether aberrant RNAs stabilized by DUX4-mediated NMD inhibition produce
82 truncated proteins by performing paired RNA-sequencing (RNA-seq) and ribosome profiling
83 (Ribo-seq) at 0, 4, 8, and 14 hours (h) following the expression of DUX4 in MB135-iDUX4
84 human skeletal muscle myoblasts, a well-characterized cellular model of FSHD [25, 26]. While
85 RNA-seq measures transcript abundance, Ribo-seq measures ribosome density along an
86 mRNA [27]. Thus, Ribo-seq serves as a proxy for active translation and allows precise
87 delineation of translation start and end sites in order to characterize the protein products made
88 from aberrant RNAs. Using Ribo-seq, we found that hundreds of aberrant RNAs, stabilized by
89 DUX4-mediated inhibition of NMD, are actively translated to produce truncated proteins –
90 particularly truncated RNA-binding proteins (RBPs) and splicing factors. We show that one such
91 truncated splicing factor, serine/arginine-rich splicing factor 3 (SRSF3-TR), is expressed in
92 FSHD muscle cell cultures and contributes to DUX4 toxicity. Thus, our findings demonstrate that
93 NMD inhibition results in the widespread production of truncated proteins with deleterious
94 cellular consequences.

RESULTS

DUX4 expression allows functional exploration of the consequences of acute NMD inhibition. Misexpression of DUX4 in skeletal muscle cells inhibits NMD and induces cytotoxicity [22, 26, 28]. To identify time points at which to measure transcript- and translation-level changes induced by DUX4 before the onset of overt cytotoxicity, we utilized a well-characterized doxycycline-inducible DUX4 human myoblast line, MB135-iDUX4 [26], harboring a DUX4-responsive mCherry fluorescent reporter (**Figure 1A**). We live imaged these cells every 15 min for 28 h following doxycycline treatment to induce DUX4 (**Figure 1A**, **Video 1**). Expression of the DUX4-responsive mCherry was rapid and nearly synchronous, with fluorescence detection after 2 h. Cytotoxicity was first observed 9 h following DUX4 induction, with most cells dead or dying by 18 h (**Video 1**). Western blot analysis showed that levels of the key NMD factor UPF1 were reduced to 47% after only 2 h of DUX4 induction and continued to decrease (**Figure 1B**). This confirmed our previous observation that NMD inhibition is an early event during DUX4 expression [23]. Given these data, we chose the time points of 4, 8, and 14 h post-DUX4 induction to investigate the consequences of NMD inhibition by DUX4.

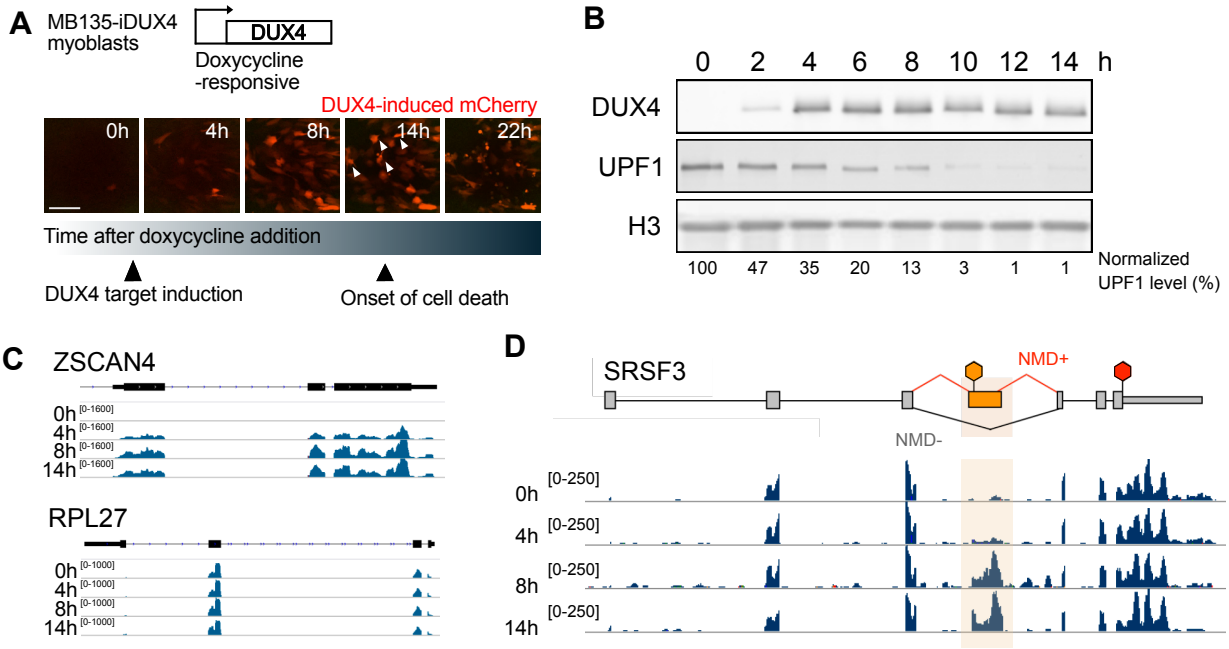

Figure 1. Synchronous expression of DUX4 in MB135-iDUX4 myoblasts enables time course analyses of downstream gene expression changes. (**A**) Representative images from live cell fluorescence microscopy of MB135-iDUX4/ZSCAN4-mCherry myoblasts following treatment with doxycycline to induce DUX4. Arrowheads indicate overtly dying cells. Scale bar, 150 µm. (**B**) Western blot analysis for DUX4, UPF1, and Histone H3 (loading control) over a time course of DUX4 expression following doxycycline induction in MB135-iDUX4 myoblasts. (**C**) RNA-seq read coverage over a time course of DUX4 expression for DUX4 target gene ZSCAN4 (top) and housekeeping gene RPL27 (bottom). (**D**) RNA-seq coverage over SRSF3. The PTC-containing exon 4 is highlighted. The red hexagon indicates the normal stop codon while the orange hexagon denotes the PTC.

111 First, we examined DUX4-induced transcriptome changes revealed by our RNA-seq dataset
112 (**Supplementary Table 1**). As expected, transcripts of a DUX4 target gene, *ZSCAN4*, were
113 absent in uninduced cells but highly expressed at 4 h and increased with time **(Figure 1C**, top),
114 while the housekeeping gene *RPL27* had constant, robust RNA expression throughout the time
115 course **(Figure 1C**, bottom). Also as expected, aberrant transcript isoforms with PTC-containing
116 exons, such as *SRSF3*, were present at very low levels prior to DUX4 expression but increased
117 in abundance thereafter, appearing as early as 4 h post-induction (**Figure 1D**).
118
119 Genome-wide, DUX4 altered the expression of thousands of transcripts, with known DUX4
120 targets [25] showing increasing upregulation throughout the time course (**Figure S1A**). Using K-
121 means clustering, we grouped the genes significantly altered (defined as absolute log2 fold
122 change > 1 and adjusted p-value < 0.01) at any point during the time course into five clusters
123 (**Figure S1B**) and carried out gene ontology (GO) analysis on each cluster (**Figure S1C**,
124 **Supplementary Table 2**). The genes rapidly induced upon DUX4 expression (Cluster 1) are
125 enriched for negative regulation of cell differentiation, positive regulation of cell proliferation, and
126 DNA-templated transcription, while those rapidly silenced upon DUX4 expression (Cluster 5) are
127 enriched for myogenesis, positive regulation of cell differentiation, and cytoskeleton
128 organization. Together, this is illustrative of a general switch away from a differentiated muscle
129 program and towards a proliferative phenotype, which is consistent with DUX4's normal role in
130 establishing an early embryonic program. Interestingly, the cluster of genes induced only at the
131 late 14 h time point (Cluster 3) is enriched for GO categories mRNA splicing, ribonucleoprotein
132 transport, ubiquitin-dependent process, unfolded protein response, and hypoxia, which have all
133 been previously reported as major signatures of DUX4-induced gene expression [22, 26, 28].
134 Together, these RNA-seq data show that the 4, 8, and 14 h time points capture the temporal
135 range of DUX4-induced gene expression changes, and are consistent with early induction of
136 transcriptional responses and late induction of cell stress response.
137
138 **Ribosome profiling shows concordance between transcript levels and ribosome**
139 **occupancy upon DUX4 expression.** Previous quantitative analysis of the DUX4-induced
140 proteome via stable isotope labeling by amino acids in cell culture (SILAC) mass spectrometry
141 showed discordant changes at the RNA versus protein level [24] raising the possibility that
142 translation could be modulated upon DUX4 expression. Additionally, at later time points DUX4
143 induces dsRNA-mediated activation of PKR [29] and stimulates PERK via the unfolded protein

144 response pathway [24], resulting in eIF2α phosphorylation, which is known to inhibit cap-
145 dependent translation [30]. Therefore, we asked whether transcript level changes driven by
146 DUX4 expression were echoed at the level of translation by comparing the RNA-seq and Ribo-
147 seq datasets.
148
149 The characteristic 3 nucleotide periodicity exhibited by the ribosome-protected RNA fragments
150 confirmed the high quality of our Ribo-seq data (**Figure S2**). Representative Ribo-seq read
151 coverage plots of the DUX4 target gene, *ZSCAN4*, showed no coverage in uninduced cells, low
152 ribosome density beginning at 4 h, and active translation at 8 and 14 h (**Figure 2A**, top). In
153 contrast, housekeeping gene *RPL27* showed constant, robust translation throughout the time
154 course (**Figure 2A**, bottom). The changes in ribosome-association at these specific genes
155 mirrored the differences seen in their mRNA levels (**Figure 1C**).
156
157 On a genome scale, DUX4 altered the translation status for thousands of transcripts, with later
158 time points showing larger differences and known DUX4 targets being translated at increasing
159 levels throughout the time course (**Figure 2B**, **Supplementary Table 3**). Most genes were
160 concordantly up or downregulated at the level of transcript and inferred translation efficiency
161 (**Figure 2C**, Materials and Methods) at all time points with only a small number of genes
162 showing some discordance. GO analysis of the discordantly regulated genes returned
163 significant results only for the gene set that showed a mild translation downregulation at the 14
164 h time point (n = 137) with pathways such as protein targeting to ER and viral transcription
165 being enriched which, strikingly, were driven entirely by a group of ribosomal protein-encoding
166 genes (**Supplementary Table 3**). This mild downregulation of translation is consistent with
167 induction of the integrated stress response (ISR) pathway and DUX4-mediated eIF2α
168 phosphorylation [24, 29]. A caveat of Ribo-seq to keep in mind here is that it may not capture
169 the true absolute change in translation efficiency induced by ISR, and therefore the translation
170 downregulation we observe could be an underestimate.
171
172 Nonetheless, we observe several hallmarks of ISR activation at 14 h, including robust
173 translation upregulation of ATF4 (**Figure 2C-D**). Specifically, the start-stop regulatory element in
174 the 5' untranslated region of ATF4, which modifies downstream re-initiation to enhance ATF4's
175 inducibility under stress [31], is highly occupied by ribosomes at 14 h (**Figure 2D**). The resultant
176 upregulation of ATF4 protein can account for the subsequent transcriptional and translational
177 induction of the ATF4 targets GADD34 and ATF3 (**Figure 2E-F**). These data confirm the DUX4-

178 induced phosphorylation of eIF2α via PKR and PERK activation culminate in a block in cap-
179 dependent translation, and stimulation of robust ISR signaling at the late 14 h time point (**Figure**
180 **2G**). Yet, in large part DUX4-induced changes in transcript level are mirrored in their ribosome
181 occupancy.

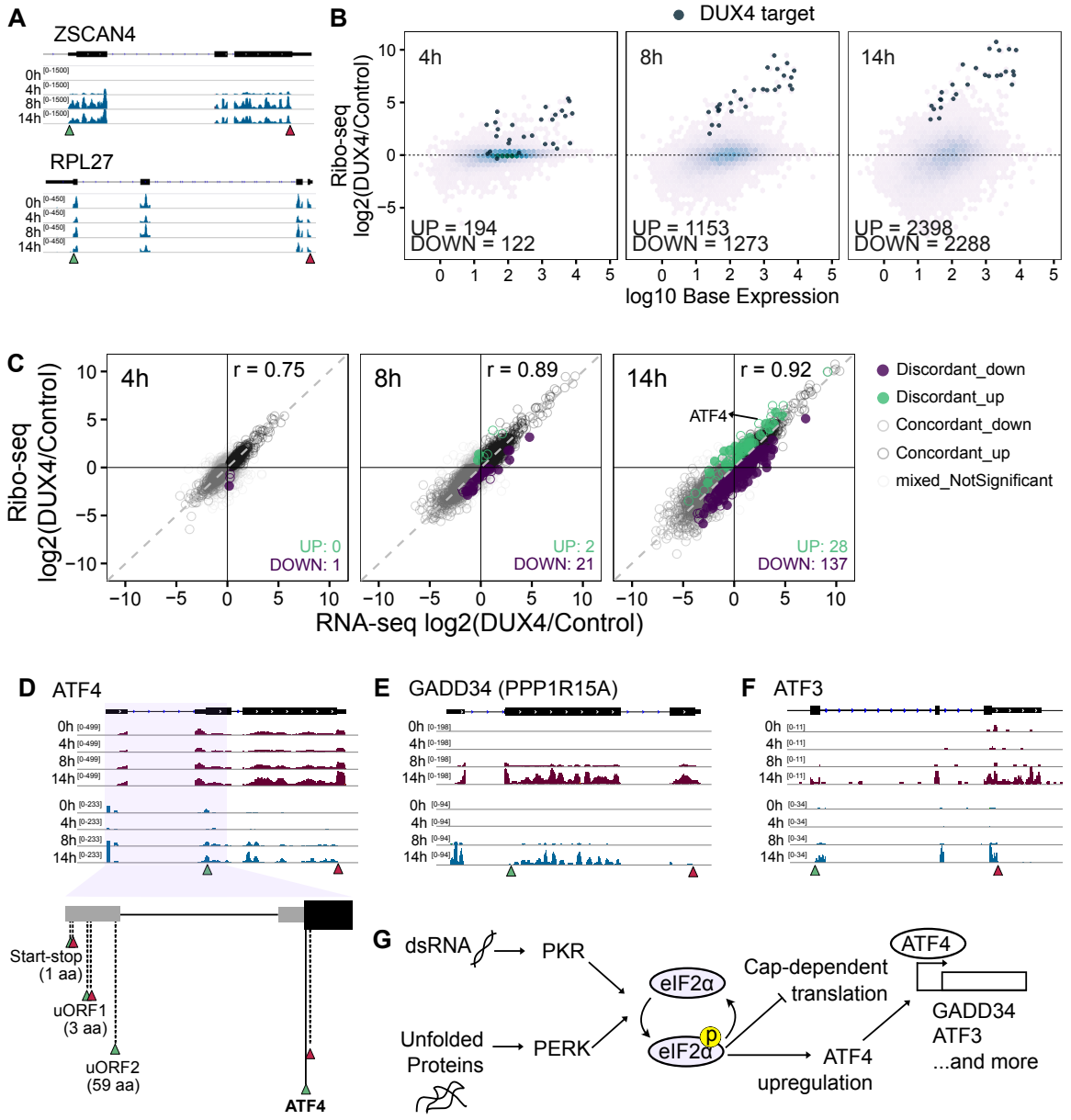

Figure 2. Ribo-seq shows high concordance between transcript levels and translation status. (**A**) Ribo-seq read coverage over a time course of DUX4 expression for DUX4 target gene ZSCAN4 (top) and housekeeping gene RPL27 (bottom). Green triangle, translation start. Red triangle, translation stop. (**B**) M-A plots for Ribo-seq data after 4, 8, and 14 h of DUX4 induction compared to the 0 h control. (**C**) Scatter plot of RNA-seq versus Ribo-seq log2 fold change after 4, 8, and 14 h of DUX4 expression. Significance defined as adjusted p-value < 0.01 for Ribo-seq fold change. (**D**) RNA-seq (top) and Ribo-seq (middle) coverage over ATF4; schematic showing the upstream (uORF) and main open reading frames of ATF4 (bottom). (**E-F**) RNA-seq (top) and Ribo-seq (bottom) coverage over GADD34 (**E**) and ATF3 (**F**). (**G**) A schematic summary of how DUX4 expression influences translation and subsequent cell stress.

182

183 **DUX4 causes widespread truncated protein production.** Having shown that most transcripts
184 induced by DUX4 are robustly translated, and that NMD inhibition is an early consequence of
185 DUX4 expression, we sought to determine whether truncated proteins are produced from PTC-
186 containing RNAs stabilized by DUX4-mediated NMD inhibition. Strikingly, when we compared
187 the RNA-seq and Ribo-seq reads at candidate genes with NMD isoforms, IVNS1ABP, SRSF3,
188 SRSF6, and SRSF7, we saw robust coverage across the PTC-containing exon with reads
189 stopping at the PTC (**Figure 3A**). This clearly indicates the translation of truncated proteins from
190 NMD isoforms.
191
192 To systematically ask if and when aberrant RNAs are translated on a genome-level, we used
193 ORFquant [32], a new pipeline that identifies isoform-specific translation events from Ribo-seq
194 data. We then used DEXSeq [33] to conduct exon-level differential analysis on the set of
195 ORFquant-derived open reading frames, using Ribo-seq data. This analysis identifies changes
196 in relative exon usage to measure differences in the expression of individual exons that are not
197 simply the consequence of changes in overall transcript level. After 4 h of DUX4 induction 397
198 genes showed differential expression of specific exons, of which 24 are predicted NMD targets
199 (**Figure 3B**), whereas later time points showed a greater number of exons (n = 96 at 14 h) that
200 are unique to NMD targets as differentially expressed (**Supplementary Table 4**). We grouped
201 exons based on their NMD target status and calculated their fold change in ribosome footprints
202 at 4, 8, and 14 h of DUX4 expression compared to the 0 h time point (**Figure 3C**). We observed
203 a progressive and significant increase in the translation status of NMD-targeted exons, but not
204 canonical exons, at 8 and 14 h, confirming the translation of stabilized aberrant RNAs in DUX4-
205 expressing cells.
206
207 Translation of an NMD target typically generates a prematurely truncated protein. To ask how
208 the specific truncated proteins being produced in DUX4-expressing myoblasts might functionally
209 impact cell homeostasis, we conducted GO analysis of the 74 truncated proteins being actively
210 translated at 14 h of DUX4 induction (**Figure 3D**, **Supplementary Table 4**). Strikingly, the
211 truncated proteins are enriched for genes encoding RBPs involved in mRNA metabolism and
212 specifically, splicing (**Supplementary Table 4**). Thus, not only are NMD targets stabilized by
213 DUX4 expression, but they also produce truncated versions of many RBPs, which could have
214 substantial downstream consequences to mRNA processing in DUX4-expressing cells.

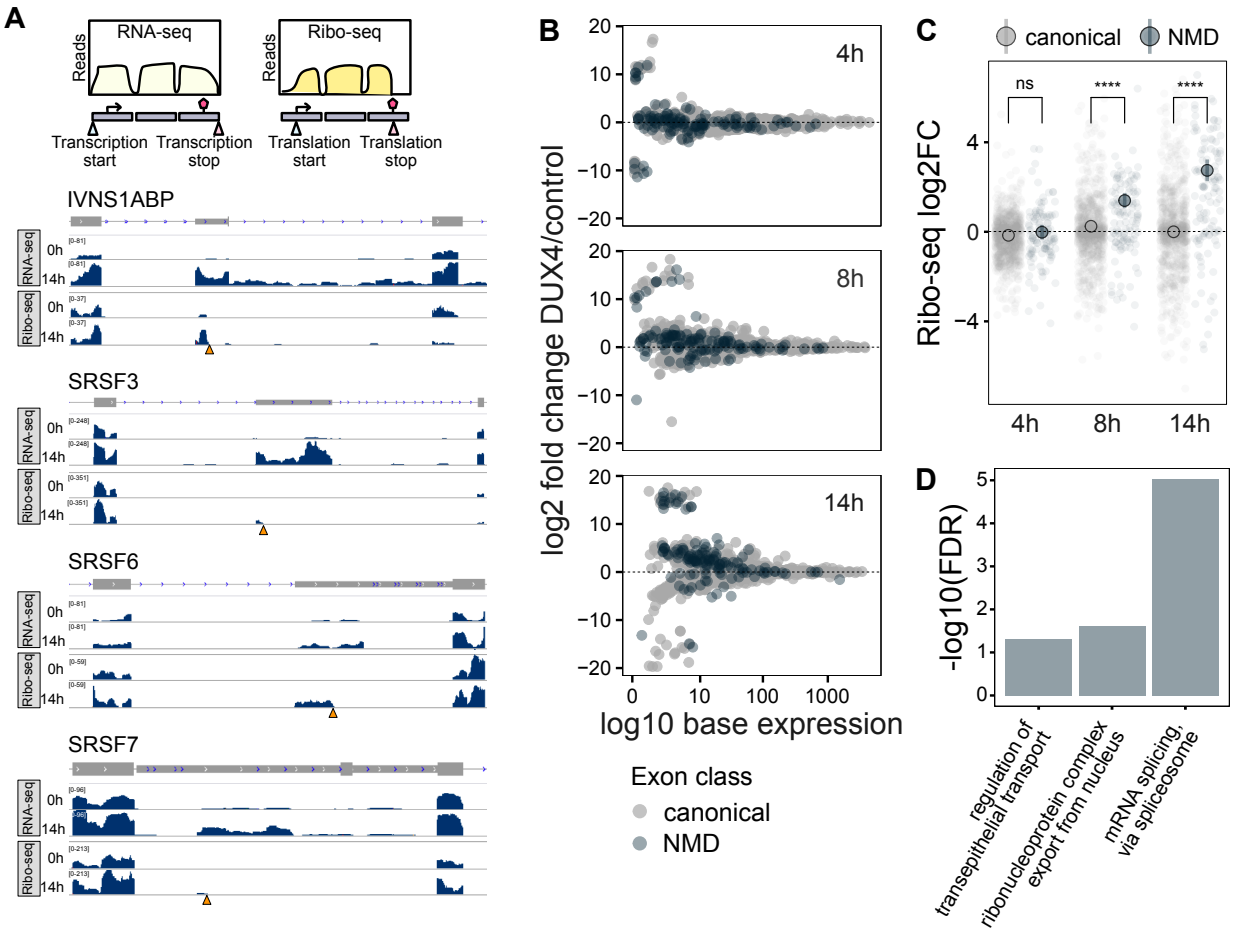

Figure 3. Exon-level analysis of *de novo* identified ORFs from Ribo-seq data demonstrates robust translation of NMD-targeted aberrant RNAs. (A) Schematic representation of the paired RNA-seq and Ribo-seq experiment (top) and RNA-seq and Ribo-seq coverage over splicing-related genes IVNS1ABP, SRSF3, SRSF6, and SRSF7 (bottom). Orange triangles denote PTCs. (**B**) M-A plot of exon-level analysis of Ribo-seq data from 4, 8, and 14 h of DUX4 induction. The x-axis represents mean expression calculated at the level of each exon within a gene. (**C**) Exon-level log2 fold change Ribo-seq values at 4, 8, or 14 h of DUX4 expression for canonical and NMD exons. Statistical testing was performed using a two-sided Wilcoxon test. (**D**) GO analysis results of selected gene sets (biological process complete) for all NMD targets that are translated at 14 h.

Truncated SRSF3 is present in FSHD myotubes and contributes to cytotoxicity. To explore the role of truncated proteins in DUX4-induced cellular phenotypes, we chose SRSF3 for further characterization. SRSF3 is an SR family protein that possesses an N-terminal RNA-binding RNA recognition motif (RRM) and a C-terminal arginine/serine (RS)-rich domain responsible for protein-protein and protein-RNA interactions. The NMD isoform of SRSF3 encodes a truncated protein (SRSF3-TR) that lacks most of the RS domain and has been previously implicated in a variety of human pathologies [34-38]. Examination of our Ribo-seq data revealed robust expression and translation of SRSF3 NMD-targeted exon 4 that ends at the site of the PTC (**Figure 4A**).

225

226 To determine the translation status of the aberrant SRSF3 transcript stabilized by DUX4, we
227 carried out polysome profiling using sucrose density gradient separation. The polysome profile
228 after 14 h of DUX4 expression compared to control showed a higher fraction of 80S compared
229 to polysomes (**Figure 4B**, top left). This is consistent with our prior observation of eIF2α
230 phosphorylation [24, 29] and resultant global downregulation of translation at 14 h. We extracted
231 RNA from various fractions and profiled RNA levels of specific transcripts by qPCR. *RPL27*
232 mRNA was predominantly ribosome-bound in control cells but this partially shifted to
233 monosomes in DUX4-expressing cells (**Figure 4B**, top right). The loss of transcripts from
234 polysome fractions was even more stark for the normal SRSF3 isoform (SRSF3 NMD-) which
235 decreased substantially in DUX4-expressing myoblasts compared to control (**Figure 4B**, bottom
236 left). In striking contrast to both RPL27 and SRSF3 NMD-, the NMD-targeted isoform of SRSF3
237 (SRSF3 NMD+) showed a massive increase in heavy polysomes in DUX4-expressing cells
238 (**Figure 4B**, bottom right). These data show that aberrant SRSF3 mRNA is being actively
239 translated into truncated protein in DUX4-expressing myoblasts and validate the ribosome
240 footprints found on the NMD+ isoform.
241

242 To determine if we could stably detect truncated SRSF3 protein in cells, we generated an
243 antibody recognizing a 10 amino acid C-terminal neo-peptide unique to SRSF3-TR. This custom
244 SRSF3-TR antibody was able to recognize FLAG-tagged SRSF3-TR exogenously expressed in
245 293T cells and endogenous SRSF3-TR immunoprecipitated from DUX4-expressing MB135-
246 iDUX4 myoblasts (**Figure 4C**). We also used a commercial SRSF3 antibody that recognizes an
247 N-terminal epitope common to both the full-length and truncated SRSF3. This antibody detected
248 both exogenously expressed full-length and truncated FLAG-SRSF3, and endogenous full-
249 length SRSF3, but was insufficient to visualize endogenous SRSF3-TR (**Figure 4C**), possibly
250 due to lower affinity for this protein isoform in an immunoprecipitation assay. To determine if
251 SRSF3-TR was present in FSHD myotubes expressing endogenous levels of DUX4, we carried
252 out immunofluorescence for SRSF3-TR or DUX4 in differentiated FSHD and control muscle
253 cells. While there was no detectable SRSF3-TR staining in control cells, in DUX4-expressing
254 FSHD cultures SRSF3-TR appeared in cytoplasmic puncta (**Figure 4D**). Thus, not only is
255 SRSF3 NMD+ isoform translated robustly in DUX4-expressing cells, its protein product, SRSF3-
256 TR can be detected in both DUX4-expressing MB135-iDUX4 myoblasts and in FSHD patient-
257 derived myotubes.

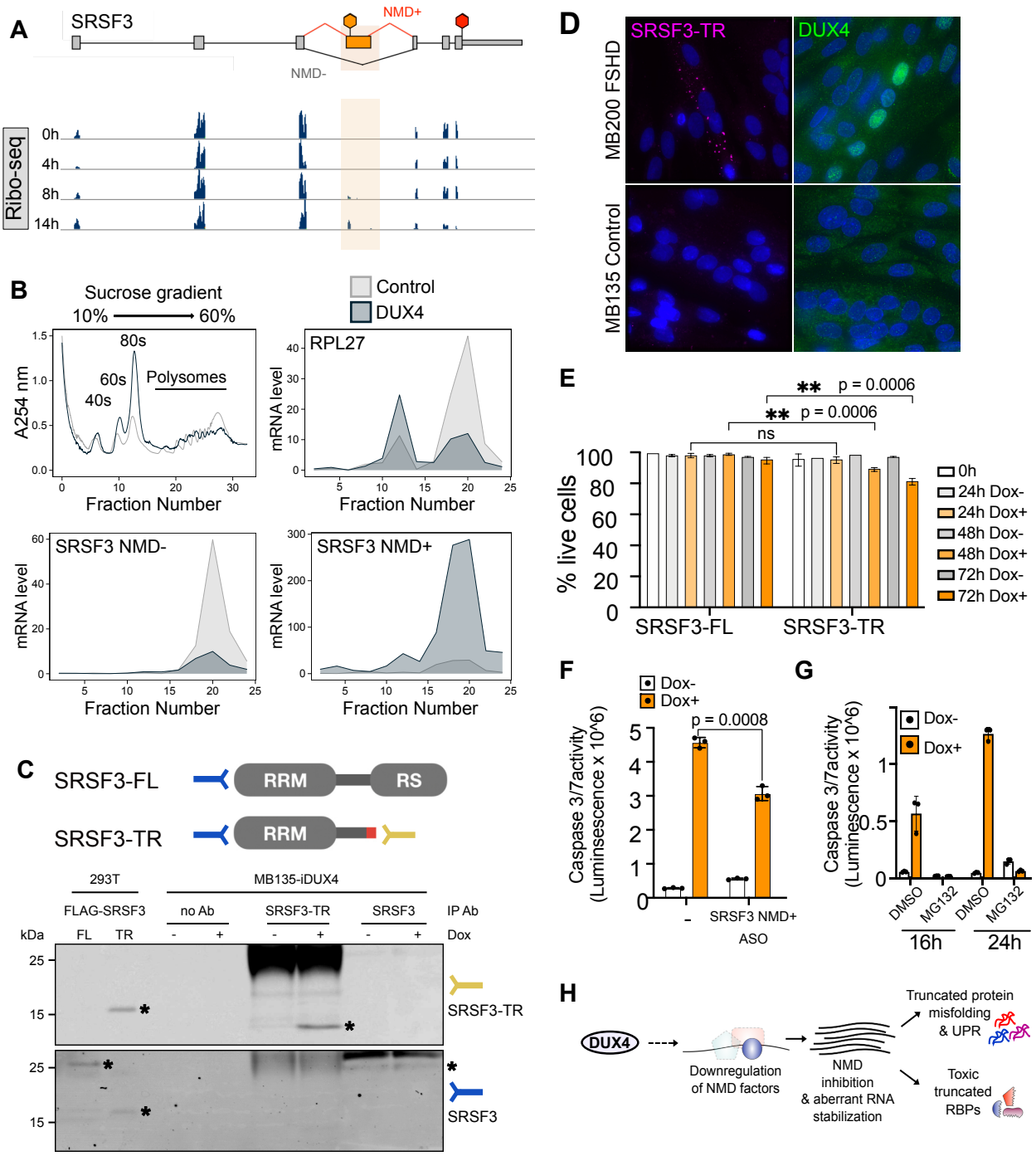

Figure 4. Truncated SRSF3 protein could disrupt RNA processing in FSHD myotubes. (**A**) Ribo-seq coverage over SRSF3. The PTC-containing exon 4 is highlighted. The red hexagon indicates the normal stop codon while the orange hexagon denotes the PTC. (**B**) Absorbance at 254 nm across a sucrose density gradient of lysates from control MB135-iDUX4 myoblasts and MB135-iDUX4 myoblasts expressing DUX4 for 14 h (top left). RT-qPCR measurement of RPL27, SRSF3 NMD-, and SRSF3 NMD+ mRNA levels in DUX4-expressing myoblasts relative to control myoblasts from collected fractions (remaining panels). (**C**) Detection of SRSF3 and SRSF3-TR in whole cell extracts from 293T cells exogenously expressing FLAG-tagged full-length (FL) or truncated (TR) SRSF3 as compared to protein lysates from MB135-iDUX4 myoblasts treated with (+) or without (-) doxycycline (Dox) to induce DUX4 and immunoprecipitated with a custom anti-SRSF3-TR antibody, no antibody (Ab), or a commercial SRSF3 antibody. IP, immunoprecipitation. Asterisks denote proteins of interest. (**D**) Immunofluorescence staining in MB135 control and MB200 FSHD myotubes differentiated for 72 h and stained with DAPI (blue) and rabbit anti-DUX4 (green)

or custom rabbit anti-SRSF3-TR (pink) antibody. (**E**) Trypan blue exclusion-based live cell counts in myoblasts expressing doxycycline (Dox)-inducible full-length (FL) or truncated (TR) SRSF3. Error bars denote the standard deviation from the mean of three biological replicates. (**F**) Caspase 3/7 activity following ASO-mediated knockdown of SRSF3 NMD+ in MB135-iDUX4 myoblasts left untreated (Dox-) or treated with doxycycline for 16 h (Dox+) to induce DUX4. Error bars denote the standard deviation from the mean of three biological replicates. (**G**) Cell viability as measured by Caspase 3/7 activity following co-treatment with doxycycline (Dox) to induce DUX4 and proteasome inhibition via MG132 treatment for 16 or 24 h. (**H**) Schematic representation of a working model where DUX4-induced downregulation of NMD factors stabilizes aberrant RNAs producing truncated RBPs and misfolded proteins that trigger the unfolded protein response and toxicity.

To ask if expression of SRSF3-TR is deleterious to cells, we exogenously expressed FLAG-tagged full-length or truncated SRSF3 in healthy muscle cells via lentiviral transduction. We found that SRSF3-TR, but not SRSF3-FL, reduced the viability of MB135 myoblasts (**Figure 4E**). To specifically knock down the SRSF3-TR isoform in DUX4-expressing myoblasts, we screened several antisense oligonucleotides (ASOs) in order to identify one (a thiomorpholino 2'-deoxyribonucleotide 3'-thiophosphate oligonucleotide chimera [39, 40]) that lowered the SRSF3-TR isoform without significantly impacting DUX4 transcript level or target expression (**Figure S3**). Treatment of DUX4-expressing myoblasts with this thiomorpholino oligonucleotide resulted in a 34% reduction in cell death compared to untreated cells (**Figure 4F**). Finally, we found that blocking the proteasome, which is the primary mediator of NMD inhibition by DUX4, robustly rescues DUX4 toxicity (**Figure 4G**). These results suggest that truncated proteins confer toxicity to muscle cells via a gain-of-function mechanism. Significantly, this mechanism is potentially additive across the different species of truncated proteins that are robustly made upon DUX4 expression in myoblasts (**Figure 4H**).

DISCUSSION

Loss of NMD leads to the stabilization of aberrant RNAs [41]. However, it is not known whether these aberrant RNAs are translated and what proteins they might produce. Here, we paired RNA-seq and Ribo-seq across a time course of DUX4 expression in human skeletal muscle myoblasts to demonstrate that DUX4-induced NMD inhibition indeed causes truncated protein production at a genome level.

The production of truncated proteins upon NMD inhibition by DUX4 has multiple implications at both molecular and functional levels. Protein truncation could result in a dominant negative function that inhibits the activity of the remaining, cell critical full-length protein. Truncated proteins might misfold and facilitate the formation of protein aggregates. And finally, some truncated proteins contain unique C-terminal extensions, or neo-peptides, that could serve as novel antigens and might induce inflammation. Hence, when NMD is modulated as a therapeutic intervention for genetic diseases, it is important to consider whether truncated proteins are produced as a consequence, and whether this might have a negative impact. In physiological contexts where NMD efficiency is suppressed without negative consequences, cells may possess mechanisms that counter truncated protein production. Further investigation of the suppression or tolerance of truncated proteins in these contexts would reveal new mechanisms that enable the protein quality control rheostat to be adjusted to deal with variable NMD efficiencies.

In FSHD, there is evidence for truncated proteins contributing to myotoxicity via all of the above mechanisms. Here, we show gain-of-function toxicity for SRSF3-TR. Prior work has demonstrated protein aggregation [29, 42, 43], as well as immune cell infiltration [44-47] in FSHD muscle. Our results suggest that these effects could be due to truncated proteins and neoantigenic epitopes. In addition, many of the identified DUX4-induced truncated proteins are RBPs and splicing factors. It is well-established that DUX4 alters RNA splicing [22, 24, 26, 28] and therefore interesting to speculate that truncated RBPs and splicing proteins might be responsible for inducing global RNA processing defects [48]. Such misprocessing would generate aberrant RNAs that could act to further overwhelm the already inhibited NMD pathway.

In summary, we demonstrate the widely-held but previously unproven assumption that NMD inhibition indeed results in the production of truncated proteins with deleterious cellular consequences. In doing so, we provide a framework to interpret the multifaceted phenotypes

307 observed in FSHD as a potential result of NMD inhibition. Our findings provide a critical missing
308 piece in the understanding of this essential quality control mechanism in both disease and
309 physiology, which has implications for treatment of genetic diseases.

310 **MATERIALS AND METHODS**

311

312 **RESOURCE AVAILABILITY**

313

314 **Lead contact**

315 Further information and requests for resources and reagents should be directed to and will be
316 fulfilled by the lead contact, Sujatha Jagannathan (sujatha.jagannathan@cuanschutz.edu).

317

318 **Materials availability**

319 The cell lines and antibody generated in this study are available upon request. Plasmids
320 generated in this study have been deposited to Addgene (plasmid #171951, #171952, #172345,
321 and #172346).

322

323 **Data and code availability**

324 The RNA-seq and Ribo-seq data generated during this study are available at GEO (accession
325 number GSE178761). The code generated during this study are available at GitHub
326 (https://github.com/sjaganna/2021-campbell_dyle_calviello_et_al).

327

328 **EXPERIMENTAL MODEL AND SUBJECT DETAILS**

329

330 **Cell lines and culture conditions**

331 293T cells were obtained from ATCC (CRL-3216). MB135, MB135-iDUX4, MB135-
332 iDUX4/ZSCAN4-mCherry, and MB200 immortalized human myoblasts were a gift from Dr.
333 Stephen Tapscott and originated from the Fields Center for FSHD and Neuromuscular
334 Research at the University of Rochester Medical Center. MB135-iDUX4 cells have been
335 described previously [26]. MB135-iFLAG-SRSF3-FL, and MB135-iFLAG-SRSF3-TR
336 immortalized human myoblasts were generated in this study. All parental cell lines were
337 authenticated by karyotype analysis and determined to be free of mycoplasma by PCR
338 screening. 293T cells were maintained in Dulbecco's Modified Eagle Medium (DMEM) (Thermo
339 Fisher Scientific) supplemented with 10% EqualFETAL (Atlas Biologicals). Myoblasts were
340 maintained in Ham's F-10 Nutrient Mix (Thermo Fisher Scientific) supplemented with 20% Fetal
341 Bovine Serum (Thermo Fisher Scientific), 10 ng/mL recombinant human basic fibroblast growth
342 factor (Promega), and 1 μM dexamethasone (Sigma-Aldrich). MB135-iDUX4/ZSCAN4-mCherry
343 and MB135-iDUX4 myoblasts were additionally maintained in 2 μg/mL puromycin

344 dihydrochloride (VWR). MB135-iFLAG-SRSF3-FL and -TR myoblasts were additionally
345 maintained in 10 µg/mL blasticidin S HCl (Thermo Fisher Scientific). Induction of DUX4 and
346 SRSF3 transgenes was achieved by culturing cells in 1-2 µg/mL doxycycline hyclate (Sigma-
347 Aldrich). Differentiation of myoblasts into myotubes was achieved by switching the fully
348 confluent myoblast monolayer into DMEM containing 1% horse serum (Thermo Fisher
349 Scientific) and Insulin-Transferrin-Selenium (Thermo Fisher Scientific). All cells were incubated
350 at 37 °C with 5% CO_2.
351
352 **METHOD DETAILS**
353
354 **Cloning**
355 pTwist-FLAG-SRSF3_Full.Length_Codon.Optimized and pTwist-FLAG-
356 SRSF3_Truncated_Codon.Optimized plasmids were synthesized by Twist Bioscience. To
357 construct pCW57.1-FLAG-SRSF3_Full.Length_Codon.Optimized-Blast and pCW57.1-FLAG-
358 SRSF3_Truncated_Codon.Optimized-Blast plasmids, the SRSF3 open reading frames were
359 subcloned into pCW57-MCS1-P2A-MCS2 (Blast) (a gift from Adam Karpf, Addgene plasmid
360 #80921) [49] by restriction enzyme digest using EcoRI and BamHI (New England Biolabs).
361
362 **Antibody generation**
363 Purified SRSF3-TR peptide (Cys-PRRRVTIMSLLTTL) was used as an immunogen and
364 polyclonal rabbit anti-SRSF3-TR antibody production was done in collaboration with Pacific
365 Immunology (Ramona, CA). The antisera from all animals were screened for reactivity by ELISA
366 against the immunogen and with western blots and immunofluorescence against transfected
367 SRSF3-TR.
368
369 **Transgenic cell line generation**
370 Lentiviral particles expressing doxycycline-inducible FLAG-SRSF3-FL or -TR transgenes were
371 generated by co-transfecting 293T cells with the appropriate lentivector, pMD2.G (a gift from
372 Didier Trono, Addgene plasmid #12259), and psPAX2 (a gift from Didier Trono, Addgene
373 plasmid #12260) using Lipofectamine 2000 Transfection Reagent (Thermo Fisher Scientific). To
374 generate polyclonal SRSF3 transgenic cell lines, MB135 myoblasts were transduced with
375 lentivirus in the presence of 8 µg/mL polybrene (Sigma-Aldrich) and selected using 10 µg/mL
376 blasticidin S HCl.
377

378 **Plasmid transfections**
379 293T cells were transfected with pTwist-FLAG-SRSF3_Full.Length_Codon.Optimized and
380 pTwist-FLAG-SRSF3_Truncated_Codon.Optimized plasmids using Lipofectamine 2000
381 Transfection Reagent following the manufacturer's instructions.
382
383 **Live cell imaging**
384 MB135-iDUX4/ZSCAN4-mCherry myoblasts were induced with doxycycline hyclate to turn on
385 DUX4 expression and subjected to time lapse imaging using the IncuCyte S3 incubator
386 microscope system (Sartorius). Images were collected every 15 min from the time of
387 doxycycline addition (t = 0 h) to 28 h.
388
389 **RNA extraction and RT-qPCR**
390 Total RNA was extracted from whole cells using TRIzol Reagent (Thermo Fisher Scientific)
391 following the manufacturer's instructions. Isolated RNA was treated with DNase I (Thermo
392 Fisher Scientific) and reverse transcribed to cDNA using SuperScript III reverse transcriptase
393 (Thermo Fisher Scientific) and random hexamers (Thermo Fisher Scientific) according to the
394 manufacturer's protocol. Quantitative PCR was carried out on a CFX384 Touch Real-Time PCR
395 Detection System (Bio-Rad) using primers specific to each gene of interest and iTaq Universal
396 SYBR Green Supermix (Bio-Rad). The expression levels of target genes were normalized to
397 that of the reference gene *RPL27* using the delta-delta-Ct method [50]. The primers used in this
398 study are listed in the Key Resources Table.
399
400 **RNA-seq library preparation and sequencing**
401 Total RNA was extracted from whole cells using TRIzol Reagent following the manufacturer's
402 instructions. Isolated RNA was subjected to ribosomal RNA depletion using the Ribo-Zero rRNA
403 Removal Kit (Illumina). RNA-seq libraries were prepared using the NEXTflex Rapid Directional
404 qRNA-Seq Kit (Bioo Scientific) following the manufacturer's instructions and sequenced using
405 75 bp single-end sequencing on the Illumina NextSeq 500 platform by the BioFrontiers Institute
406 Next-Gen Sequencing Core Facility.
407
408 **Ribosome footprinting**
409 Ribo-seq was performed as described previously [32] using six 70% confluent 10 cm dishes of
410 MB135-iDUX4 cells per condition. Briefly, cells were washed with ice-cold phosphate-buffered
411 saline (PBS) supplemented with 100 µg/mL cycloheximide (Sigma-Aldrich), flash frozen on

412 liquid nitrogen, and lysed in Lysis Buffer (PBS containing 1% (v/v) Triton X-100 and 25 U/mL
413 TurboDNase (Ambion)). Cells were harvested by scraping and further lysed by trituration ten
414 times through a 26-gauge needle. The lysate was clarified by centrifugation at 20,000 g for 10
415 min at 4 °C. The supernatants were flash frozen in liquid nitrogen and stored at -80 °C. Thawed
416 lysates were treated with RNase I (Ambion) at 2.5 U/µL for 45 min at room temperature with
417 gentle mixing. Further RNase activity was stopped by addition of SUPERaseIn RNase Inhibitor
418 (Thermo Fisher Scientific). Next, ribosome complexes were enriched using MicroSpin S-400 HR
419 Columns (GE Healthcare) and RNA extracted using the Direct-zol RNA Miniprep Kit (Zymo
420 Research). Ribo-Zero rRNA Removal Kit was used to deplete rRNAs and the ribosome-
421 protected fragments were recovered by running them in a 17% Urea gel, staining with SYBR
422 Gold (Invitrogen), and extracting nucleic acids that are 27 to 30 nucleotides long from gel slices
423 by constant agitation in 0.3 M NaCl at 4 °C overnight. The recovered nucleic acids were
424 precipitated with isopropanol using GlycoBlue Coprecipitant (Ambion) as carrier and treated with
425 T4 polynucleotide kinase (Thermo Fisher Scientific). Libraries were prepared using the
426 NEXTflex Small RNA-Seq Kit v3 (Bioo Scientific) following the manufacturer's instructions and
427 sequenced using 75 bp single-end reads on an Illumina NextSeq 500 by the BioFrontiers
428 Institute Next-Gen Sequencing Core Facility.
429
430 **RNA-seq and Ribo-seq data analysis**
431 Fastq files were stripped of the adapter sequences using cutadapt. UMI sequences were
432 removed, and reads were collapsed to fasta format. Reads were first aligned against rRNA
433 (accession number U13369.1), and to a collection of snoRNAs, tRNAs, and miRNA (retrieved
434 using the UCSC table browser) using bowtie2 [51]. Remaining reads were mapped to the hg38
435 version of the genome (without scaffolds) using STAR 2.6.0a [52] supplied with the GENCODE
436 25 .gtf file. A maximum of two mismatches and mapping to a minimum of 50 positions was
437 allowed. De-novo splice junction discovery was disabled for all datasets. Only the best
438 alignment per each read was retained. Quality control and read counting of the Ribo-seq data
439 was performed with Ribo-seQC [53].
440
441 Differential gene expression analysis of the RNA-seq data was conducted using DESeq2 [54].
442 Briefly, featureCounts from the subread R package [55] was used to assign aligned reads (in
443 BAM format) to genomic features supplied with the GENCODE 25. gtf file. The featureCounts
444 output was then supplied to DESeq2 and differential expression analysis was conducted with
445 the 0 h time point serving as the reference sample. Genes with very low read count were filtered

446 out by requiring at least a total of 10 reads across the 12 samples (3 replicates each of the 0, 4,
447 8, and 14 h samples). Log2 fold change shrinkage was done using the apeglm function [56].
448
449 Differential analysis of the RNA-seq and Ribo-seq data was performed using DESeq2, as
450 previously described [57, 58], using an interaction model between the tested condition and
451 RNA-seq – Ribo-seq counts. Only reads mapping uniquely to coding sequence regions were
452 used. In addition, ORFquant [32] was used to derive de-novo isoform-specific translation
453 events, by pooling the Ribo-seQC output from all Ribo-seq samples, using uniquely mapping
454 reads. DEXSeq [33] was used to perform differential exon usage along the DUX4 time course
455 data, using Ribo-seq counts on exonic bins and junctions belonging to different ORFquant-
456 derived translated regions. NMD candidates were defined by ORFquant as open reading frames
457 ending with a stop codon upstream of an exon-exon junction.
458
459 **GO category analysis**
460 Gene Ontology (GO) analysis was conducted using the web tool http://geneontology.org,
461 powered by pantherdb.org. Briefly, statistical overrepresentation test using the complete GO
462 biological process annotation dataset was conducted and p-values were calculated using the
463 Fisher's exact test and False Discovery Rate was calculated by the Benjamini-Hochberg
464 procedure.
465
466 **Polysome profiling**
467 Polysome profiling was performed as previously described [59, 60] with the following
468 modifications. Four 70% confluent 15 cm dishes of MB135-iDUX4 cells per condition were
469 treated with 100 µg/mL cycloheximide for 10 min, transferred to wet ice, washed with ice-cold
470 PBS containing 100 µg/mL cycloheximide, and then lysed in 400 µL Lysis Buffer (20 mM
471 HEPES pH 7.4, 15 mM $MgCl_2$, 200 mM NaCl, 1% Triton X-100, 100 µg/mL cycloheximide, 2
472 mM DTT, and 100 U/mL SUPERaseIn RNase Inhibitor) per 15 cm dish. The cells and buffer
473 were scraped off the dish and centrifuged at 13,000 rpm for 10 min at 4 °C. Lysates were
474 fractionated on a 10% to 60% sucrose gradient using the SW 41 Ti Swinging-Bucket Rotor
475 (Beckman Coulter) at 36,000 rpm for 3 h and 10 min. Twenty-four fractions were collected using
476 a Gradient Station ip (BioComp) and an FC 203B Fraction Collector (Gilson) with continuous
477 monitoring of absorbance at 254 nm. RNA from each fraction was extracted using TRIzol LS
478 Reagent (Thermo Fisher Scientific) following the manufacturer's instructions. RT-qPCR was
479 carried out as described above.

480

481 **Protein extraction**

482 Total protein was extracted from whole cells using TRIzol Reagent following the manufacturer's
483 instructions, excepting that protein pellets were dissolved in Protein Resuspension Buffer (0.5 M
484 Tris base, 5% SDS). Isolated protein was quantified using the Pierce BCA Protein Assay Kit
485 (Thermo Fisher Scientific) according to the manufacturer's protocol. Protein was mixed with 4X
486 NuPAGE LDS Sample Buffer (Thermo Fisher Scientific) containing 50 mM DTT and heated to
487 70 °C before immunoblotting.

488

489 **Immunoprecipitation**

490 MB135-iDUX4 myoblasts were treated with or without doxycycline for 14 h and then trypsinized
491 prior to lysis on ice in 1 mL of Lysis Buffer (50 mM Tris-HCl pH 7.5, 150 mM NaCl, 1% NP-40)
492 containing protease inhibitors (Sigma Aldrich). Lysates were precleared using Protein G
493 Sepharose (Thermo Fisher Scientific) for 1 h prior to an overnight incubation at 4 °C with either
494 anti-SRSF3 or anti-SRSF3-TR antibody. Protein G Sepharose was added the following morning
495 for 5 h to bind the antibody, and beads were subsequently washed 5 times with 1 mL cold Lysis
496 Buffer. After the final wash, 4X NuPAGE LDS Sample Buffer containing 50 mM DTT was added
497 directly to the beads and samples heated to 70 °C for protein elution before immunoblotting.

498

499 **Immunoblotting**

500 Protein was run on NuPAGE Bis-Tris precast polyacrylamide gels (Thermo Fisher Scientific)
501 alongside PageRuler Plus Prestained Protein Ladder (Thermo Fisher Scientific) and transferred
502 to Odyssey nitrocellulose membrane (LI-COR Biosciences). Membranes were blocked in
503 Intercept (PBS) Blocking Buffer (LI-COR Biosciences) before overnight incubation at 4 °C with
504 primary antibodies diluted in Blocking Buffer containing 0.2% Tween 20. Membranes were
505 incubated with IRDye-conjugated secondary antibodies (LI-COR Biosciences) for 1 h and
506 fluorescent signal visualized using a Sapphire Biomolecular Imager (Azure Biosystems) and
507 Sapphire Capture software (Azure Biosystems). When appropriate, membranes were stripped
508 with Restore Western Blot Stripping Buffer (Thermo Fisher Scientific) before being re-probed.
509 Band intensities were quantified by densitometry using ImageJ [61].

510

511 **Immunofluorescence**

512 Cells were fixed in 10% Neutral Buffered Formalin (Research Products International) for 30 min
513 and permeabilized for 10 min in PBS with 0.1% Triton X-100. Samples were then incubated

514 overnight at 4 °C with primary antibodies, followed by incubation with 488- or 594-conjugated
515 secondary antibodies for 1 h prior to counterstaining and mounting with Prolong Diamond
516 Antifade Mountant with DAPI (Thermo Fisher Scientific). Slides were imaged with a DeltaVision
517 Elite deconvolution microscope, CoolSNAP HQ^2 high-resolution CCD camera, and Resolve3D
518 softWoRx-Acquire v7.0 software. Image J software [61] was used for image analysis.
519
520 **Solid phase synthesis of TMO chimeras (ASOs)**
521 TMO chimeras were synthesized according to the previously reported procedure [39, 40].
522 Briefly, the 5'-dimethoxytrityl (DMT) protecting group of the solid supported 2'-
523 deoxyribonucleoside (CPG-500 support, Glen Research) was deprotected in the first stage by
524 using 3% trichloroacetic acid in dichloromethane. In the second stage, condensation of the
525 resulting CPG-500 support linked 5'-hydroxyl-2'-deoxyribonucleoside with the 6'-DMT-
526 morpholinonucleoside 3'-phosphordiamidites of mA^{Bz}, mG^{iBu}, mC^{Bz}, mT (ChemGenes) or
527 commercial 2'-deoxyribonucleoside 3'-phosphoramidites was achieved using 5-ethylthio-1H-
528 tetrazole (ETT) in anhydrous acetonitrile as activator (30 sec condensation time). Subsequent
529 conversion of P(III) linkages to P(V) thiophosphoramidate (TMO) or P(V) 2'-deoxyribonucleoside
530 3'-thiophosphate was achieved by using 3-[(Dimethylaminomethylene)amino]-3H-1,2,4-
531 dithiazole-5-thione (DDTT) as the sulfurization agent. Finally, the unreacted hydroxyl groups
532 were acetylated by conventional capping reagents (Cap A: Tetrahydrofuran/Acetic Anhydride
533 and Cap B: 16% 1-Methylimidazole in Tetrahydrofuran; Glen Research). The 5'-DMT protecting
534 group on the resulting dinucleotide was next deprotected using deblocking mixture and this
535 DMT deprotected dinucleotide was then used for additional cycles in order to generate ASOs
536 having internucleotide thiophosphoramidate or thiophosphate linkages. The above cycle was
537 repeated to provide the thiomorpholino oligonucleotide chimeras of the desired length and
538 sequence. Cleavage of these 5'-protected DMT-on oligonucleotides from the solid support and
539 deprotection of base and phosphorus protecting groups was carried out using 0.5 mL of 28%
540 aqueous ammonia at 55 °C for 16 h. Subsequently, the CPG was filtered through a micro spin
541 centrifuge filter with pore size of 0.2 µm and the resulting filtrate was evaporated to dryness on a
542 SpeedVac (Thermo Fisher Scientific). The residue was dissolved in 0.75 mL of 3%
543 acetonitrile/water mixture and filtered through a micro spin centrifuge filter. A small portion of the
544 crude sample was withdrawn and submitted to LCMS analysis. The remaining reaction mixture
545 was purified by RP-HPLC. Fractions containing the pure ASO were combined, evaporated to
546 dryness, and submitted to LCMS analysis. Fractions containing the pure DMT-on ASO were
547 dissolved in 0.5 mL of detritylation mixture. After 25 min at 40 °C, the mixture was neutralized

548 with 5 µL of triethylamine, filtered using a micro spin centrifuge filter, and the filtrate containing
549 the sample was purified by RP-HPLC column chromatography. Fractions containing the final
550 DMT-off product were combined and evaporated to dryness on a SpeedVac. The residue was
551 submitted to LCMS analysis in order to determine the purity of the sample. The concentration of
552 the ASO was determined by NanoDrop spectrophotometry before storing the samples at -20 °C.
553
554 **LCMS analysis**
555 LCMS analysis was performed on an Agilent 6530 series Q-TOF LC/MS spectrometer. A
556 Waters ACQUITY UPLC® BEH C18, 1.7 µm, 2.1 X 100 nm column was used as the stationary
557 phase. Aqueous phase was Buffer A (950 mL water, 25 mL methanol, 26 mL hexafluoro-2-
558 propanol (HFIP) and 2.5 mL triethyl amine) and organic phase was Buffer B (925 mL methanol,
559 50 mL water, 26 mL hexafluoro-2-propanol (HFIP) and 2.5 mL triethyl amine). The gradient was
560 0-100% of Buffer B for 30 min followed by 100% Buffer B for 5 min at a flow rate of 0.2 mL/min
561 and a set temperature of 25 °C. The observed masses of the ASOs were consistent with the
562 expected theoretical masses.
563
564 **Antisense oligonucleotide transfections**
565 ASOs were transfected into MB135-iDUX4 cells 40 h prior to doxycycline induction using
566 Lipofectamine RNAiMAX Transfection Reagent (Thermo Fisher Scientific) following the
567 manufacturer's instructions. The ASOs used in this study are listed in the Key Resources Table.
568
569 **Cell viability assays**
570 Trypan blue dye was used to determine the viability of MB135-iFLAG-SRSF3-FL and -TR cell
571 lines. Ten microliters of trypsinized and resuspended cells were mixed with 10 µL of 0.4%
572 Trypan Blue Stain (Thermo Fisher Scientific) for 1 min before immediate counting using a
573 hemocytometer and Motic AE2000 inverted light microscope. Caspase 3/7 activity was used to
574 determine the viability of MB135-iDUX4 myoblasts treated with ASOs or proteasome inhibitors.
575 MB135-iDUX4 cells were seeded in 24-well plates at 8e4 cells per well, transfected with ASOs
576 as described above, and 40 h later treated with 2 µg/mL doxycycline hyclate or seeded in 96-
577 well plates at 3e3 cells per well and 24 h later treated with 1 µg/mL doxycycline hyclate and
578 either DMSO or 10 µM MG132 (Sigma-Aldrich). Caspase 3/7 activity was measured 16 and 24
579 h later using the Caspase-Glo 3/7 Assay System (Promega) following the manufacturer's
580 instructions. Luminescence was detected using a GloMax-Multi Detection System (Promega).
581

582 **Antibodies**

583 The antibodies used in this study are anti-DUX4 (Abcam 124699), anti-Histone H3 (Abcam
584 1791), anti-SRSF3 (Thermo Fisher Scientific 33-4200), anti-SRSF3-TR (this paper), anti-
585 RENT1/hUPF1 (Abcam ab109363), Drop-n-Stain CF 488A Donkey Anti-Rabbit IgG (Biotium
586 20950), Drop-n-Stain CF 594 Donkey Anti-Rabbit IgG (Biotium 20951), IRDye 650 Goat anti-
587 Mouse IgG Secondary Antibody (LI-COR Biosciences 926-65010), and IRDye 800CW Goat
588 anti-Rabbit IgG Secondary Antibody (LI-COR Biosciences 926-32211).

589

590 **QUANTIFICATION AND STATISTICAL ANALYSIS**

591

592 **Data analysis, statistical tests, and visualization**

593 All data analysis and statistical tests were performed in the R programming environment and
594 relied on Bioconductor [62] and ggplot2 [63]. Plots were generated using R plotting functions
595 and/or the ggplot2 package. Bar graphs were generated using GraphPad Prism software
596 version 9.0. Biological replicates were defined as experiments performed separately on distinct
597 samples (i.e. cells cultured in different wells) representing identical conditions and/or time
598 points. No outliers were eliminated in this study. Statistical tests were performed using R
599 functions or GraphPad Prism.

ACKNOWLEDGEMENTS

We thank Stephen Tapscott for the MB135-iDUX4/ZSCAN4-mCherry cell line. We thank Jeffrey Kieft for his guidance in carrying out polysome profiling. We thank Neelanjan Mukherjee, Olivia Rissland, Srinivas Ramachandran, and all members of the Jagannathan laboratory for insightful manuscript feedback. We thank the BioFrontiers Institute Next-Gen Sequencing Core Facility, which performed the Illumina sequencing and library construction. This work was supported by the RNA Bioscience Initiative, University of Colorado Anschutz Medical Campus (S.J.), the University of Colorado Boulder (K.S. and M.H.C.), Friends of FSH Research and The Chris Carrino Foundation for FSHD AWD-194864 (S.J.), the National Institutes of Health grant R35GM133433 (S.J.), the FSHD Society FSHS-82018-01 (A.E.C. and M.D.), the California Tobacco-Related Disease Research Grants Program 27KT-0003 (S.N.F.), and the National Institutes of Health DP2GM132932 (S.N.F.).

AUTHOR CONTRIBUTIONS

A.E.C., M.C.D., and S.J. conceived and designed the study. A.E.C, M.C.D., M.A.C., and T.F. performed experiments. K.S. and M.H.C. provided the thiomorpholino oligonucleotides. A.E.C., L.C., T.M., R.F., A.E.G., M.H.C., S.N.F., and S.J. analyzed data. A.E.C. and S.J. wrote the paper with input from all authors.

DECLARATION OF INTERESTS

The authors declare no competing interests.

621 **SUPPLEMENTAL FILES**

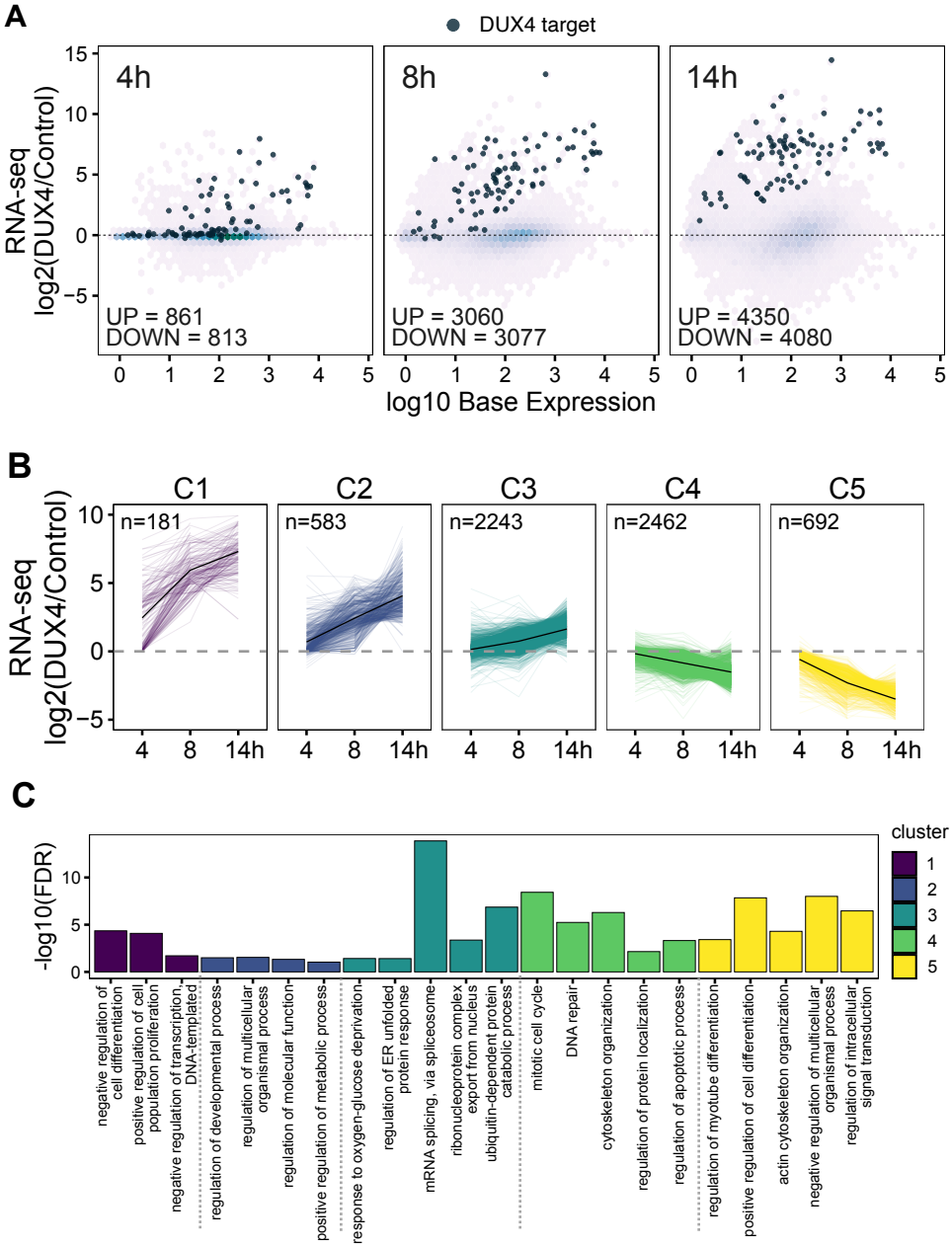

Figure S1. Time course RNA-seq in MB135-iDUX4 myoblasts reveals early transcript-level changes in pathways underlying FSHD pathology. (**A**) M-A plots for RNA-seq data after 4, 8, and 14 h of DUX4 induction compared to the 0 h control. DUX4 target status defined as in [25]. (**B**) Log2 fold change in RNA expression from the 0 h time point is shown for each gene after k-means clustering. The thick black line represents the cluster mean. (**C**) GO analysis results of selected gene sets (biological process complete) that are significantly enriched in each cluster defined in (**B**).

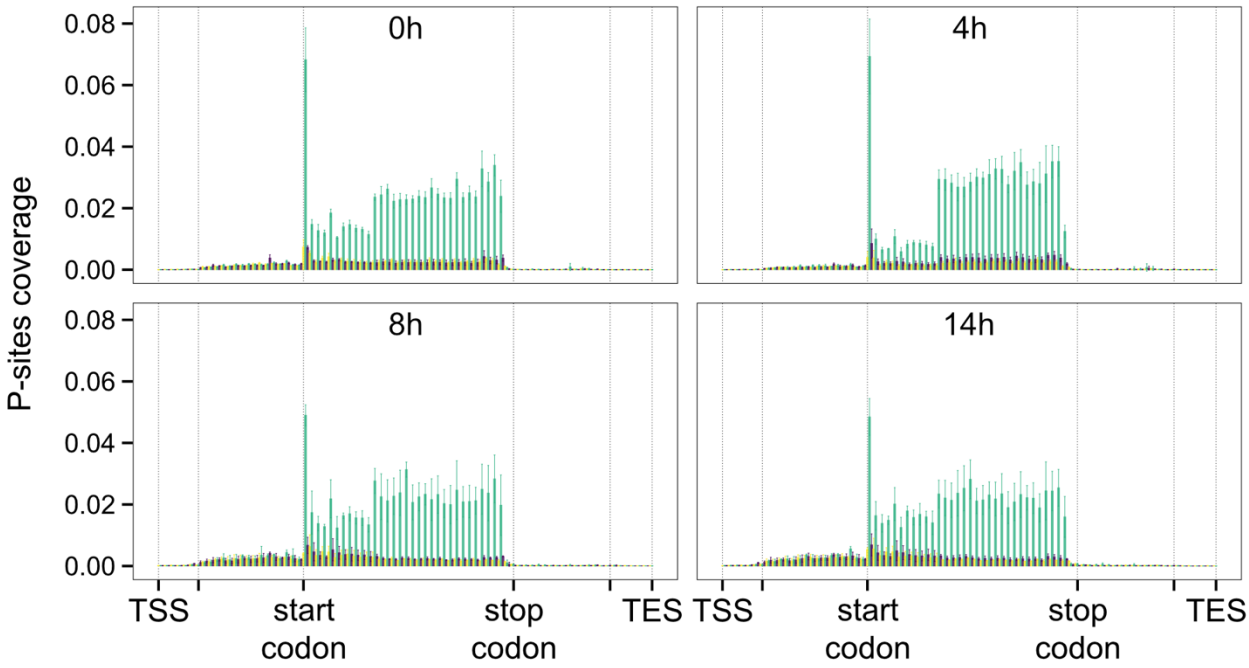

Figure S2. Ribo-seq quality control. Aggregate profile of P-sites coverage (as calculated by Ribo-seQC) depicting single nucleotide resolution of Ribo-seq data along the time course. Each frame is shown with a different color. Error bars represent the standard deviation from three biological replicates.

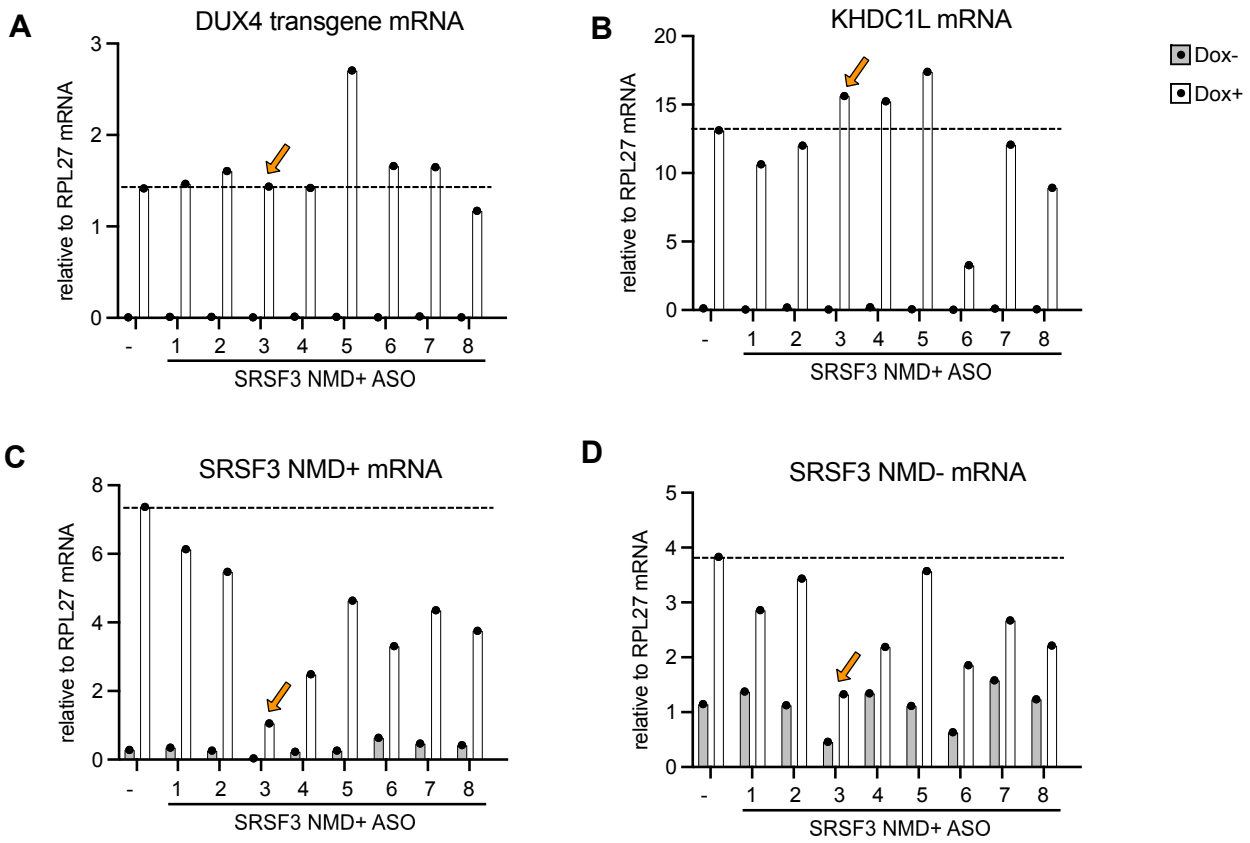

Figure S3. Relative RNA levels of (**A**) DUX4 transgene, (**B**) KHDC1L (DUX4 target gene), (**C**) SRSF3 NMD+, and (**D**) SRSF3 NMD- isoforms as determined by RT-qPCR following transfection with antisense oligos (ASOs) targeting SRSF3 NMD+ and doxycycline (Dox) treatment for 14 h to induce DUX4 in MB135-iDUX4 myoblasts. The tested ASOs are numbered 1-8; "-" indicates no ASO control. The orange arrow indicates the ASO chosen for further studies in Figure 4F.

622 **Video 1. Time course imaging following DUX4 expression.**
623 Live cell fluorescence microscopy recording of MB135-iDUX4/ZSCAN4-mCherry myoblasts
624 treated with doxycycline to induce DUX4 expression.
625
626 **Supplementary Table 1.**
627 DESeq2 differential gene expression analysis results for DUX4 time course RNA-seq data at 4,
628 8, or 14 h post-induction compared to 0 h (control).
629
630 **Supplementary Table 2.**
631 Cluster analysis of RNA-seq log2 fold change at 4, 8, or 14 h of DUX4 induction compared to 0
632 h (control); and Gene Ontology analysis of genes within each cluster.
633
634 **Supplementary Table 3.**
635 ORFquant analysis results for DUX4 time course RNA-seq and Ribo-seq data at 4, 8, or 14 h
636 post-induction compared to 0 h (control); and Gene Ontology analysis of genes with
637 downregulated ribosome density at 14 h.
638
639 **Supplementary Table 4.**
640 DEXSeq analysis results for DUX4 time course Ribo-seq data at 4, 8, or 14 h post-induction
641 compared to 0 h (control); and Gene Ontology analysis of NMD targets upregulated at 14 h.

642 **REFERENCES**

643

644 1. Mendell JT, Sharifi NA, Meyers JL, Martinez-Murillo F, Dietz HC. Nonsense surveillance
645 regulates expression of diverse classes of mammalian transcripts and mutes genomic noise.
646 Nat Genet. 2004;36(10):1073-8. https://doi.org/10.1038/ng1429

647 2. Lareau LF, Inada M, Green RE, Wengrod JC, Brenner SE. Unproductive splicing of SR
648 genes associated with highly conserved and ultraconserved DNA elements. Nature.
649 2007;446(7138):926-9. https://doi.org/10.1038/nature05676

650 3. Ni JZ, Grate L, Donohue JP, Preston C, Nobida N, O'Brien G, et al. Ultraconserved
651 elements are associated with homeostatic control of splicing regulators by alternative splicing
652 and nonsense-mediated decay. Genes Dev. 2007;21(6):708-18.
653 http://www.genesdev.org/cgi/doi/10.1101/gad.1525507

654 4. Li Z, Vuong JK, Zhang M, Stork C, Zheng S. Inhibition of nonsense-mediated RNA
655 decay by ER stress. RNA. 2017;23(3):378-94.
656 http://www.rnajournal.org/cgi/doi/10.1261/rna.058040.116

657 5. Barberan-Soler S, Lambert NJ, Zahler AM. Global analysis of alternative splicing
658 uncovers developmental regulation of nonsense-mediated decay in C. elegans. RNA.
659 2009;15(9):1652-60. https://doi.org/10.1261/rna.1711109

660 6. Bruno IG, Karam R, Huang L, Bhardwaj A, Lou CH, Shum EY, et al. Identification of a
661 microRNA that activates gene expression by repressing nonsense-mediated RNA decay. Mol
662 Cell. 2011;42(4):500-10. https://doi.org/10.1016/j.molcel.2011.04.018

663 7. Gong C, Kim YK, Woeller CF, Tang Y, Maquat LE. SMD and NMD are competitive
664 pathways that contribute to myogenesis: effects on PAX3 and myogenin mRNAs. Genes Dev.
665 2009;23(1):54-66. http://www.genesdev.org/cgi/doi/10.1101/gad.1717309

666 8. Usuki F, Yamashita A, Kashima I, Higuchi I, Osame M, Ohno S. Specific inhibition of
667 nonsense-mediated mRNA decay components, SMG-1 or Upf1, rescues the phenotype of

668 Ullrich disease fibroblasts. Mol Ther. 2006;14(3):351-60.
669 https://doi.org/10.1016/j.ymthe.2006.04.011

670 9. Huang L, Shum EY, Jones SH, Lou CH, Dumdie J, Kim H, et al. A Upf3b-mutant mouse
671 model with behavioral and neurogenesis defects. Mol Psychiatry. 2018;23(8):1773-86.
672 https://doi.org/10.1038/mp.2017.173

673 10. Karousis ED, Gypas F, Zavolan M, Muhlemann O. Nanopore sequencing reveals
674 endogenous NMD-targeted isoforms in human cells. Genome Biol. 2021;22(1):223.
675 https://doi.org/10.1186/s13059-021-02439-3

676 11. Colombo M, Karousis ED, Bourquin J, Bruggmann R, Muhlemann O. Transcriptome-
677 wide identification of NMD-targeted human mRNAs reveals extensive redundancy between
678 SMG6- and SMG7-mediated degradation pathways. RNA. 2017;23(2):189-201.
679 http://www.rnajournal.org/cgi/doi/10.1261/rna.059055.116

680 12. Pastor F, Kolonias D, Giangrande PH, Gilboa E. Induction of tumour immunity by
681 targeted inhibition of nonsense-mediated mRNA decay. Nature. 2010;465(7295):227-30.
682 https://doi.org/10.1038/nature08999

683 13. Becker JP, Helm D, Rettel M, Stein F, Hernandez-Sanchez A, Urban K, et al. NMD
684 inhibition by 5-azacytidine augments presentation of immunogenic frameshift-derived
685 neoepitopes. iScience. 2021;24(4):102389. https://doi.org/10.1016/j.isci.2021.102389

686 14. Tawil R, van der Maarel SM, Tapscott SJ. Facioscapulohumeral dystrophy: the path to
687 consensus on pathophysiology. Skelet Muscle. 2014;4:12. https://doi.org/10.1186/2044-5040-4-
688 12

689 15. Hamel J, Tawil R. Facioscapulohumeral muscular dystrophy: update on pathogenesis
690 and future treatments. Neurotherapeutics. 2018;15(4):863-71. https://doi.org/10.1007/s13311-
691 018-00675-3

692 16. De Iaco A, Planet E, Coluccio A, Verp S, Duc J, Trono D. DUX-family transcription
693 factors regulate zygotic genome activation in placental mammals. Nat Genet. 2017;49(6):941-5.
694 https://doi.org/10.1038/ng.3858

695 17. Hendrickson PG, Dorais JA, Grow EJ, Whiddon JL, Lim JW, Wike CL, et al. Conserved
696 roles of mouse DUX and human DUX4 in activating cleavage-stage genes and MERVL/HERVL
697 retrotransposons. Nat Genet. 2017;49(6):925-34. https://doi.org/10.1038/ng.3844

698 18. Whiddon JL, Langford AT, Wong CJ, Zhong JW, Tapscott SJ. Conservation and
699 innovation in the DUX4-family gene network. Nat Genet. 2017;49(6):935-40.
700 https://doi.org/10.1038/ng.3846

701 19. Kowaljow V, Marcowycz A, Ansseau E, Conde CB, Sauvage S, Matteotti C, et al. The
702 DUX4 gene at the FSHD1A locus encodes a pro-apoptotic protein. Neuromuscul Disord.
703 2007;17(8):611-23. https://doi.org/10.1016/j.nmd.2007.04.002

704 20. Bosnakovski D, Xu Z, Gang EJ, Galindo CL, Liu M, Simsek T, et al. An isogenetic
705 myoblast expression screen identifies DUX4-mediated FSHD-associated molecular pathologies.
706 EMBO J. 2008;27(20):2766-79. https://doi.org/10.1038/emboj.2008.201

707 21. Wallace LM, Garwick SE, Mei W, Belayew A, Coppee F, Ladner KJ, et al. DUX4, a
708 candidate gene for facioscapulohumeral muscular dystrophy, causes p53-dependent myopathy
709 in vivo. Ann Neurol. 2011;69(3):540-52. https://doi.org/10.1002/ana.22275

710 22. Rickard AM, Petek LM, Miller DG. Endogenous DUX4 expression in FSHD myotubes is
711 sufficient to cause cell death and disrupts RNA splicing and cell migration pathways. Hum Mol
712 Genet. 2015;24(20):5901-14. https://doi.org/10.1093/hmg/ddv315

713 23. Feng Q, Snider L, Jagannathan S, Tawil R, van der Maarel SM, Tapscott SJ, et al. A
714 feedback loop between nonsense-mediated decay and the retrogene DUX4 in
715 facioscapulohumeral muscular dystrophy. Elife. 2015;4. https://doi.org/10.7554/eLife.04996

716 24. Jagannathan S, Ogata Y, Gafken PR, Tapscott SJ, Bradley RK. Quantitative proteomics
717 reveals key roles for post-transcriptional gene regulation in the molecular pathology of
718 facioscapulohumeral muscular dystrophy. Elife. 2019;8. https://doi.org/10.7554/eLife.41740

719 25. Yao Z, Snider L, Balog J, Lemmers RJ, Van Der Maarel SM, Tawil R, et al. DUX4-
720 induced gene expression is the major molecular signature in FSHD skeletal muscle. Hum Mol
721 Genet. 2014;23(20):5342-52. https://doi.org/10.1093/hmg/ddu251

722 26. Jagannathan S, Shadle SC, Resnick R, Snider L, Tawil RN, van der Maarel SM, et al.
723 Model systems of DUX4 expression recapitulate the transcriptional profile of FSHD cells. Hum
724 Mol Genet. 2016;25(20):4419-31. https://doi.org/10.1093/hmg/ddw271

725 27. Ingolia NT. Ribosome profiling: new views of translation, from single codons to genome
726 scale. Nat Rev Genet. 2014;15(3):205-13. https://doi.org/10.1038/nrg3645

727 28. Geng LN, Yao Z, Snider L, Fong AP, Cech JN, Young JM, et al. DUX4 activates
728 germline genes, retroelements, and immune mediators: implications for facioscapulohumeral
729 dystrophy. Dev Cell. 2012;22(1):38-51. https://doi.org/10.1016/j.devcel.2011.11.013

730 29. Shadle SC, Zhong JW, Campbell AE, Conerly ML, Jagannathan S, Wong CJ, et al.
731 DUX4-induced dsRNA and MYC mRNA stabilization activate apoptotic pathways in human cell
732 models of facioscapulohumeral dystrophy. PLoS Genet. 2017;13(3):e1006658.
733 https://doi.org/10.1371/journal.pgen.1006658

734 30. Proud CG. eIF2 and the control of cell physiology. Semin Cell Dev Biol. 2005;16(1):3-12.
735 https://doi.org/10.1016/j.semcdb.2004.11.004

736 31. Rendleman J, Mohammad MP, Pressler M, Maity S, Hronová V, Gao Z, et al. Regulatory
737 start-stop elements in 5' untranslated regions pervasively modulate translation. bioRxiv. 2021.
738 https://doi.org/10.1101/2021.07.26.453809

739 32. Calviello L, Hirsekorn A, Ohler U. Quantification of translation uncovers the functions of
740 the alternative transcriptome. Nat Struct Mol Biol. 2020;27(8):717-25.
741 https://doi.org/10.1038/s41594-020-0450-4

742 33. Anders S, Reyes A, Huber W. Detecting differential usage of exons from RNA-seq data.
743 Genome Res. 2012;22(10):2008-17. http://www.genome.org/cgi/doi/10.1101/gr.133744.111

744 34. More DA, Kumar A. SRSF3: Newly discovered functions and roles in human health and
745 diseases. Eur J Cell Biol. 2020;99(6):151099. https://doi.org/10.1016/j.ejcb.2020.151099

746 35. Zhou Z, Gong Q, Lin Z, Wang Y, Li M, Wang L, et al. Emerging roles of SRSF3 as a
747 therapeutic target for cancer. Front Oncol. 2020;10:577636.
748 https://doi.org/10.3389/fonc.2020.577636

749 36. Kano S, Nishida K, Nishiyama C, Akaike Y, Kajita K, Kurokawa K, et al. Truncated
750 serine/arginine-rich splicing factor 3 accelerates cell growth through up-regulating c-Jun
751 expression. J Med Invest. 2013;60(3-4):228-35. https://doi.org/10.2152/jmi.60.228

752 37. Kano S, Nishida K, Kurebe H, Nishiyama C, Kita K, Akaike Y, et al. Oxidative stress-
753 inducible truncated serine/arginine-rich splicing factor 3 regulates interleukin-8 production in
754 human colon cancer cells. Am J Physiol Cell Physiol. 2014;306(3):C250-62.
755 https://doi.org/10.1152/ajpcell.00091.2013

756 38. Jimenez M, Urtasun R, Elizalde M, Azkona M, Latasa MU, Uriarte I, et al. Splicing
757 events in the control of genome integrity: role of SLU7 and truncated SRSF3 proteins. Nucleic
758 Acids Res. 2019;47(7):3450-66. https://doi.org/10.1093/nar/gkz014

759 39. Langner HK, Jastrzebska K, Caruthers MH. Synthesis and characterization of
760 thiophosphoramidate morpholino oligonucleotides and chimeras. J Am Chem Soc.
761 2020;142(38):16240-53.https://doi.org/10.1021/jacs.0c04335

762 40. Paul S, Caruthers MH. Synthesis of backbone modified morpholino oligonucletodies and
763 chimeras using phosphoramidite chemistry. 2022. U.S. Patent No. 11,230,565 B2.

764 41. Kurosaki T, Maquat LE. Nonsense-mediated mRNA decay in humans at a glance. J Cell
765 Sci. 2016;129(3):461-7. https://doi.org/10.1242/jcs.181008

766 42. Homma S, Beermann ML, Boyce FM, Miller JB. Expression of FSHD-related DUX4-FL
767 alters proteostasis and induces TDP-43 aggregation. Ann Clin Transl Neurol. 2015;2(2):151-66.
768 https://doi.org/10.1002/acn3.158

769 43. Homma S, Beermann ML, Yu B, Boyce FM, Miller JB. Nuclear bodies reorganize during
770 myogenesis in vitro and are differentially disrupted by expression of FSHD-associated DUX4.
771 Skelet Muscle. 2016;6(1):42. https://doi.org/10.1186/s13395-016-0113-7

772 44. Frisullo G, Frusciante R, Nociti V, Tasca G, Renna R, Iorio R, et al. CD8(+) T cells in
773 facioscapulohumeral muscular dystrophy patients with inflammatory features at muscle MRI. J
774 Clin Immunol. 2011;31(2):155-66. https://doi.org/10.1007/s10875-010-9474-6

775 45. Arahata K, Ishihara T, Fukunaga H, Orimo S, Lee JH, Goto K, et al. Inflammatory
776 response in facioscapulohumeral muscular dystrophy (FSHD): immunocytochemical and
777 genetic analyses. Muscle Nerve Suppl. 1995;2:S56-66. https://doi.org/10.1002/mus.880181312

778 46. Hauerslev S, Orngreen MC, Hertz JM, Vissing J, Krag TO. Muscle regeneration and
779 inflammation in patients with facioscapulohumeral muscular dystrophy. Acta Neurol Scand.
780 2013;128(3):194-201. https://doi.org/10.1111/ane.12109

781 47. Tasca G, Pescatori M, Monforte M, Mirabella M, Iannaccone E, Frusciante R, et al.
782 Different molecular signatures in magnetic resonance imaging-staged facioscapulohumeral
783 muscular dystrophy muscles. PLoS One. 2012;7(6):e38779.
784 https://doi.org/10.1371/journal.pone.0038779

785 48. Desai A, Hu Z, French CE, Lloyd JPB, Brenner SE. Networks of splice factor regulation
786 by unproductive splicing coupled with nonsense mediated mRNA decay. bioRxiv. 2020.
787 https://doi.org/10.1101/2020.05.20.107375

788 49. Barger CJ, Branick C, Chee L, Karpf AR. Pan-cancer analyses reveal genomic features
789 of FOXM1 overexpression in cancer. Cancers (Basel). 2019;11(2).
790 https://doi.org/10.3390/cancers11020251

791 50. Livak KJ, Schmittgen TD. Analysis of relative gene expression data using real-time
792 quantitative PCR and the 2(-Delta Delta C(T)) method. Methods. 2001;25(4):402-8.
793 https://doi.org/10.1006/meth.2001.1262

794 51. Langmead B, Salzberg SL. Fast gapped-read alignment with Bowtie 2. Nat Methods.
795 2012;9(4):357-9. https://doi.org/10.1038/nmeth.1923

796 52. Dobin A, Davis CA, Schlesinger F, Drenkow J, Zaleski C, Jha S, et al. STAR: ultrafast
797 universal RNA-seq aligner. Bioinformatics. 2013;29(1):15-21.
798 https://doi.org/10.1093/bioinformatics/bts635

799 53. Calviello L, Sydow D, Harnett D, Ohler U. Ribo-seQC: comprehensive analysis of
800 cytoplasmic and organellar ribosome profiling data. bioRxiv. 2019.
801 https://doi.org/10.1101/601468

802 54. Love MI, Huber W, Anders S. Moderated estimation of fold change and dispersion for
803 RNA-seq data with DESeq2. Genome Biol. 2014;15(12):550. https://doi.org/10.1186/s13059-
804 014-0550-8

805 55. Liao Y, Smyth GK, Shi W. featureCounts: an efficient general purpose program for
806 assigning sequence reads to genomic features. Bioinformatics. 2014;30(7):923-30.
807 https://doi.org/10.1093/bioinformatics/btt656

808 56. Zhu A, Ibrahim JG, Love MI. Heavy-tailed prior distributions for sequence count data:
809 removing the noise and preserving large differences. Bioinformatics. 2019;35(12):2084-92.
810 https://doi.org/10.1093/bioinformatics/bty895

811 57. Calviello L, Venkataramanan S, Rogowski KJ, Wyler E, Wilkins K, Tejura M, et al. DDX3
812 depletion represses translation of mRNAs with complex 5' UTRs. Nucleic Acids Res.
813 2021;49(9):5336-50. https://doi.org/10.1093/nar/gkab287

814 58. Chothani S, Adami E, Ouyang JF, Viswanathan S, Hubner N, Cook SA, et al. deltaTE:
815 Detection of translationally regulated genes by integrative analysis of Ribo-seq and RNA-seq
816 data. Curr Protoc Mol Biol. 2019;129(1):e108. https://doi.org/10.1002/cpmb.108

817 59. Merrick WC, Hensold JO. Analysis of eukaryotic translation in purified and semipurified
818 systems. Curr Protoc Cell Biol. 2001;Chapter 11:Unit 11 9.
819 https://doi.org/10.1002/0471143030.cb1109s08

820 60. Miura P, Andrews M, Holcik M, Jasmin BJ. IRES-mediated translation of utrophin A is
821 enhanced by glucocorticoid treatment in skeletal muscle cells. PLoS One. 2008;3(6):e2309.
822 https://doi.org/10.1371/journal.pone.0002309

823 61. Schneider CA, Rasband WS, Eliceiri KW. NIH Image to ImageJ: 25 years of image
824 analysis. Nat Methods. 2012;9(7):671-5. https://doi.org/10.1038/nmeth.2089

825 62. Huber W, Carey VJ, Gentleman R, Anders S, Carlson M, Carvalho BS, et al.
826 Orchestrating high-throughput genomic analysis with Bioconductor. Nat Methods.
827 2015;12(2):115-21. https://doi.org/10.1038/nmeth.3252

828 63. Wickham H. ggplot2: Elegant graphics for data analysis. New York, NY: Springer-Verlag;
829 2016.

830 64. Shadle SC, Bennett SR, Wong CJ, Karreman NA, Campbell AE, van der Maarel SM, et
831 al. DUX4-induced bidirectional HSATII satellite repeat transcripts form intranuclear double-
832 stranded RNA foci in human cell models of FSHD. Hum Mol Genet. 2019;28(23):3997-4011.
833 https://doi.org/10.1093/hmg/ddz242
834

835 **APPENDIX**

836

837 **KEY RESOURCES TABLE**

Reagent type (species) or resource	Designation	Source or reference	Identifiers	Additional information
cell line (*Homo sapiens*)	293T	ATCC	CRL-3216, RRID:CVCL_0063	
cell line (*H. sapiens*)	MB135	Stephen Tapscott		Female control myoblast line
cell line (*H. sapiens*)	MB135-iDUX4	[26]		Harbors doxycycline-inducible DUX4 transgene
cell line (*H. sapiens*)	MB135-iDUX4/ZSCAN4-mCherry	Stephen Tapscott		Harbors doxycycline-inducible DUX4 transgene and DUX4-responsive fluorescent reporter
cell line (*H. sapiens*)	MB135-iFLAG-SRSF3-FL	This paper		Harbors doxycycline-inducible, FLAG-tagged, codon-optimized, full-length SRSF3
cell line (*H. sapiens*)	MB135-iFLAG-SRSF3-TR	This paper		Harbors doxycycline-inducible, FLAG-tagged, codon-optimized, truncated SRSF3
cell line (*H. sapiens*)	MB200	Stephen Tapscott		Male FSHD myoblast line
antibody	anti-DUX4 (Rabbit monoclonal)	Abcam	ab124699, RRID:AB_10973363	IF(1:200), WB(1:1000)
antibody	anti-Histone H3 (Rabbit polyclonal)	Abcam	ab1791, RRID:AB_302613	WB(1:5000)
antibody	anti-SRSF3 (Mouse monoclonal)	Thermo Fisher Scientific	33-4200, RRID:AB_2533119	WB(1:250)
antibody	anti-SRSF3-TR (Rabbit polyclonal)	This paper		IF(1:200), WB(1:500)
antibody	anti-RENT1/hUPF1 (Rabbit monoclonal)	Abcam	ab109363, RRID:AB_10861979	WB(1:1000)
recombinant DNA reagent	pCW57.1-FLAG-SRSF3_Full.Length_Codon.Optimized-Blast (plasmid)	This paper		All-in-one lentiviral vector for doxycycline-inducible expression of FLAG-

				tagged, codon-optimized, full-length SRSF3
recombinant DNA reagent	pCW57.1-FLAG-SRSF3_Truncated_Codon.Optimized-Blast (plasmid)	This paper		All-in-one lentiviral vector for doxycycline-inducible expression of FLAG-tagged, codon-optimized, truncated SRSF3
recombinant DNA reagent	pCW57-MCS1-P2A-MCS2 (Blast) (plasmid)	Addgene	Plasmid #80921, RRID:Addgene_80921	
recombinant DNA reagent	pMD2.G (plasmid)	Addgene	Plasmid #12259; RRID:Addgene_12259	
recombinant DNA reagent	psPAX2 (plasmid)	Addgene	Plasmid #12260; RRID:Addgene_12260	
recombinant DNA reagent	pTwist-FLAG-SRSF3_Full.Length_Codon.Optimized (plasmid)	This paper		For expression of FLAG-tagged, codon-optimized full-length SRSF3 in mammalian cells; synthesized by Twist Bioscience
recombinant DNA reagent	pTwist-FLAG-SRSF3_Truncated_Codon.Optimized (plasmid)	This paper		For expression of FLAG-tagged, codon-optimized truncated SRSF3 in mammalian cells; synthesized by Twist Bioscience
sequence-based reagent	DUX4 transgene F	[64]	qPCR primers	TAGGGGAAGAGGTAGACGGC
sequence-based reagent	DUX4 transgene R	[64]	qPCR primers	CGGTTCCGGGATTCCGATAG
sequence-based reagent	KHDC1L F	[26]	qPCR primers	CACCAATGGCAAAGCAGTGG
sequence-based reagent	KHDC1L R	[26]	qPCR primers	TCAGTCTCCGGTGTACGGTG
sequence-based reagent	SRSF3 F	[23]	qPCR primers	TGGAACTGTCGAATGGTGAA
sequence-based reagent	SRSF3 NMD- R	[23]	qPCR primers	CTTGGAGATCTGCGACGAG

sequence-based reagent	SRSF3 NMD+ R	[23]	qPCR primers	GGGTGGTGAGAAGAG ACATGA
sequence-based reagent	SRSF3_TMO-11	This paper	antisense oligonucleotide	G*A*T*G*G*t*g*a*c*t*c*t* g*c*g*A*C*G*A*g (*, thiophosphoramidate or thiophosphate internucleotide linkage; capital letter, morpholino nucleoside; lowercase letter, 2'deoxynucleoside)
sequence-based reagent	RPL27 F	[26]	qPCR primers	GCAAGAAGAAGATCGC CAAG
sequence-based reagent	RPL27 R	[26]	qPCR primers	TCCAAGGGGATATCCA CAGA
peptide, recombinant protein	Insulin-Transferrin-Selenium	Thermo Fisher Scientific	41400045	
peptide, recombinant protein	Protein G Sepharose	Thermo Fisher Scientific	101241	
peptide, recombinant protein	Recombinant human basic fibroblast growth factor	Promega	G5071	
chemical compound, drug	Blasticidin S HCl	Thermo Fisher Scientific	R21001	
chemical compound, drug	Cycloheximide	Sigma-Aldrich	239765	
chemical compound, drug	Doxycycline hyclate	Sigma-Aldrich	D9891	
chemical compound, drug	Lipofectamine 2000 Transfection Reagent	Thermo Fisher Scientific	11668-030	
chemical compound, drug	Lipofectamine RNAiMAX Transfection Reagent	Thermo Fisher Scientific	13778-150	
chemical compound, drug	MG132	Sigma-Aldrich	474790	

chemical compound, drug	Puromycin dihydrochloride	VWR	97064-280	
chemical compound, drug	TRIzol Reagent	Thermo Fisher Scientific	15596018	
commerical assay or kit	BCA Protein Assay Kit	Pierce	23225	
commerical assay or kit	Caspase-Glo 3/7 Assay System	Promega	G8091	
commerical assay or kit	Direct-zol RNA Miniprep Kit	Zymo Research	R2051	
commerical assay or kit	NEXTflex Rapid Directional qRNA-Seq Kit	Bioo Scientific	NOVA-5130-02D	
commerical assay or kit	NEXTflex Small RNA-Seq Kit v3	Bioo Scientific	NOVA-5132-06	
commerical assay or kit	Ribo-Zero rRNA Removal Kit	Illumina	MRZH11124, discontinued	
commerical assay or kit	SuperScript III First-Strand Synthesis System	Thermo Fisher Scientific	18080051	
software, algorithm	Code used for RNA-seq and Ribo-seq figure generation	This paper		The code used for the RNA-seq and Ribo-seq figure generation can be accessed via github at https://github.com/sjaganna/2021-campbell_dyle_calviello_et_al
software, algorithm	GraphPad Prism	GraphPad Prism (https://graphpad.com)	RRID:SCR_002798	Version 9
software, algorithm	ImageJ	ImageJ (https://imagej.nih.gov)	RRID:SCR_003070	